Characteristics of the SOL turbulence structure in the first experimental campaign on W7-X with limiter configuration

S. C. Liu, Y. Liang, P. Drews, A. Krämer-Flecken, X. Han, D. Nicolai, G. Satheeswaran, N. C. Wang, J. Q. Cai, A. Charl, J. Cosfeld, Y. Gao, O. Grulke, M. Henkel, K. P. Hollfeld, C. Killer, A. Knieps, R. König, O. Neubauer, M. Rack, N. Sandri, S. Sereda, B. Schweer, E. H. Wang, Y. L. Wei, and W7-X Team

Citation: Physics of Plasmas **25**, 072502 (2018); doi: 10.1063/1.5033353

View online: https://doi.org/10.1063/1.5033353

View Table of Contents: http://aip.scitation.org/toc/php/25/7

Published by the American Institute of Physics

Characteristics of the SOL turbulence structure in the first experimental campaign on W7-X with limiter configuration

S. C. Liu,[1,2,a)] Y. Liang,[2] P. Drews,[2] A. Krämer-Flecken,[2] X. Han,[1,2] D. Nicolai,[2] G. Satheeswaran,[2] N. C. Wang,[3] J. Q. Cai,[1,2] A. Charl,[2] J. Cosfeld,[2] Y. Gao,[2] O. Grulke,[4] M. Henkel,[2] K. P. Hollfeld,[2] C. Killer,[4] A. Knieps,[2] R. König,[4] O. Neubauer,[2] M. Rack,[2] N. Sandri,[2] S. Sereda,[2] B. Schweer,[2] E. H. Wang,[1,2] Y. L. Wei,[2] and W7-X Team[b)]

[1]*Institute of Plasma Physics, Chinese Academy of Sciences, Hefei 230031, People's Republic of China*
[2]*Forschungszentrum Jülich GmbH, Institut für Energie- und Klimaforschung – Plasmaphysik, Partner of the Trilateral Euregio Cluster (TEC), 52425 Jülich, Germany*
[3]*State Key Laboratory of Advanced Electromagnetic Engineering and Technology, Huazhong University of Science and Technology, Wuhan, Hubei 430074, People's Republic of China*
[4]*Max-Planck-Institute for Plasma Physics, 17491 Greifswald, Germany*

(Received 5 April 2018; accepted 5 June 2018; published online 3 July 2018)

In the first experimental campaign of Wendelstein 7-X (W7-X), a combined probe head mounted on the multi-purpose manipulator has been used to measure the scrape-off layer (SOL) turbulence characteristics. The preliminary experimental results are summarized to illustrate the SOL turbulence properties in the limiter configuration on W7-X. In a standard limiter configuration, significant electrostatic fluctuations can be found in the near SOL, and the dominant frequency of fluctuation power is below 100 kHz. The auto-correlation spectrum power law decay factor is $\alpha \approx -1$ below 40 kHz and $\alpha \approx -2$ between 50 and 200 kHz. A broadband spectrum appears between 240 and 380 kHz with a low spectral power density, but a high cross-correlation coefficient. The statistical characteristics of turbulence are calculated by the two-point cross-correlation technique. A clear poloidal dispersion relation is found in the spectrum $S(k_\theta, f)$, propagating along the ion diamagnetic drift direction with a group velocity (below 100 kHz) about 0.56 km/s in the near SOL in the laboratory frame. The poloidal correlation length is around 5–10 mm in SOL. The turbulence phase velocity is about 0.5–1 km/s when close to the last closed flux surface, which is comparable with the poloidal $E \times B$ drift speed. https://doi.org/10.1063/1.5033353

I. INTRODUCTION

Turbulence plays an important role in the cross-field transport and the plasma confinement in fusion devices.[1] The anomalous transport is considered to be dominated by turbulence, which causes the particles and the energy to flow out of the nested magnetic field structure at a high rate.[2] The low frequency drift wave is one of the mechanisms to drive this cross-field transport.[3] An electrostatic coherent mode near the electron diamagnetic frequency observed in EAST tokamak can drive a significant heat and particle outflow, which is a great benefit of maintaining the long high confinement mode sustainment.[4] In the stellarator of H-1 Heliac, the turbulent transport induced by a low frequency coherent mode dominates the particle balance during the low density phase.[5] The energy transfer induced by turbulence is also important in the plasma confinement and instabilities in tokamak and stellarator. During L-H transition, the nonlinear Reynolds stress is considered to transfer energy from turbulence to low frequency turbulence-driven flows (such as zonal flow).[6,7] The energy can be transferred not only from small scale fluctuations to large scale fluctuations via a direct cascade but also from a large scale to a small scale.[7,8] In consequence, it is crucially important to study the turbulence structures and its induced transport on a fusion device with various plasma conditions.

W7-X is a new generation of optimized stellarator with a superconducting coil system to accommodate the flexible 3D magnetic configurations, aiming to achieve a quasi-steady state operation with plasma parameters close to the future fusion power plant. Its averaged major radius is 5.5 m, and the averaged minor radius is 0.5 m.[9] During the first experimental operation phase (OP1.1) of W7-X, the turbulence behaviours have been measured by various diagnostics, such as poloidal correlation reflectometry (PCR),[10,11] electron cyclotron emission (ECE),[12,13] and Mirnov coils,[14] where both the PCR and ECE measurements are located in the core plasma, and Mirnov coil is a global measurement of magnetic fluctuations. A combined probe head consisting of Langmuir probes and magnetic coils is also used in OP1.1 to measure the localized turbulence structures in the scrape-off layer (SOL). In this paper, the characteristics of SOL turbulence measured by this combined probe head in OP1.1 will be presented. The rest of the paper is structured as follows: The setups of the probe head and the manipulator are provided in Sec. II. Experimental results and discussion are described in Sec. III. Section IV is the conclusion.

II. DIAGNOSTICS SETUP

From the OP1.1, a multi-purpose manipulator (MPM) is installed in W7-X to accommodate different probe heads,

[a)]Email: sh.liu@fz-juelich.de.
[b)]Members of the W7-X Team are listed in R. C. Wolf *et al.* Nucl. Fusion **57**, 102020 (2017).

samples, and gas injection nozzles. This MPM is located at the W7-X port of AEK40 with 167 mm below the outer mid-plane. The maximum plunge distance of the fast movement of MPM is 350 mm, with a maximum acceleration of 30 m/s^2 and a speed of 3.5 m/s.[15,16] The plunge distance is measured by two laser sensors. The length of the combined probe head is 150 mm, and the parking position in OP1.1 is about $R = 6.345$ m, while the last closed surface flux (LCFS) in a standard limiter is about $R = 6.03$ m along the path of the probe, as shown on the left top panel of Fig. 1. The combined probe head consists of Langmuir probes, a Mach probe, and two tri-axial pick-up coils, which is able to measure the electron density, the electron temperature, the plasma potential, the radial electric field, the parallel flow velocity, and the variation of magnetic fields in the direction of (R, φ, Z).[17,18] The combined probe head and the arrangement of Langmuir pins are presented in Fig. 1. Here, the radial correlation is derived from "ϕ_{f1}" and "ϕ_{f3}" which are separated by 6 mm radially. When the biasing voltage of a triple-probe is switched off, the poloidal correlation is obtained between the two pins of "ϕ_{f1}" and "ϕ_p" separated by 5.2 mm poloidally. The temporal resolution of the probe system is 1 MHz. The two pick-up coils inside the combined probe head are 1.75 and 5.12 cm away from the front surface of Langmuir pins along the radial direction, respectively.

III. EXPERIMENTAL RESULTS AND DISCUSSION

A. The auto-correlation spectrum

The plasma conditions and auto-correlation spectra of discharge 160224031 are shown in Fig. 2. Note that 160224031 is the MDSplus shot number, and the corresponding W7-X program ID is 20160224.031. In Fig. 2(b), the electron cyclotron resonance heating (ECRH) power is about 3.3 MW, and the line integrated density is around 1.7–2.5 $\times 10^{19}$ m^{-2} during the plunge of the combined probe. Because there is no feedback control of the line integrated density in OP1.1, the plasma density increases slightly with time. Note that currents of the five trim coils are 995, 308, –806, –805, and 308 A in sequence for this discharge. The magnetic equilibrium is the standard limiter configuration of OP1.1 with the last closed flux surface (LCFS) located at $R = 6.03$ m in the cross section of the manipulator, as illustrated in Fig. 1. Figure 2(a) is the floating potential measured

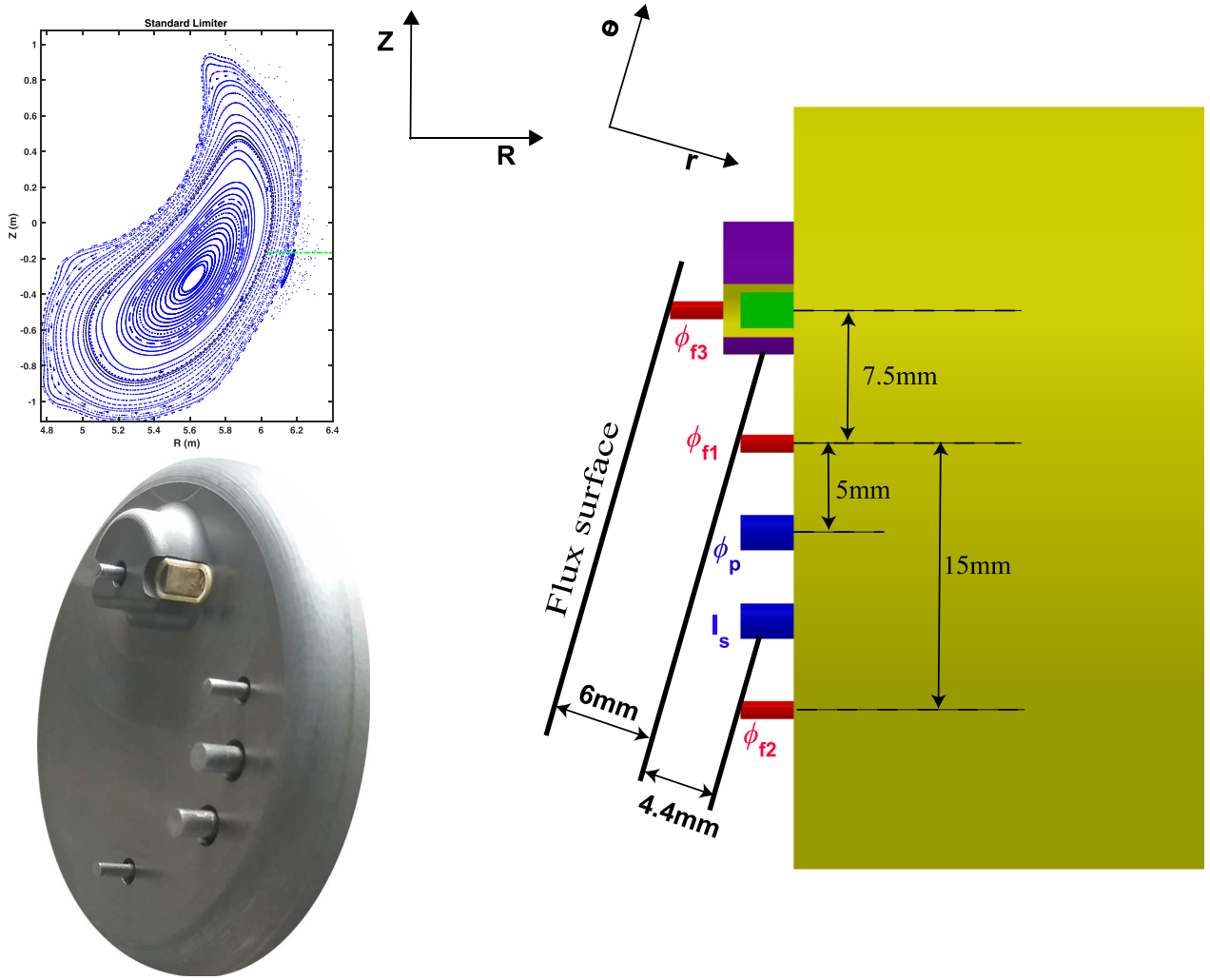

FIG. 1. The sketch of the combined probe head used in OP1.1 on W7-X. The left top panel is the Poincaré plot of a standard limiter configuration with the probe path highlighted in the green dashed line; the left bottom panel is the combined probe head; the right panel is the arrangement of Langmuir probes, "ϕ_f" is the floating potential, and "ϕ_p" is the potential on the positive side of the biasing voltage of the triple-probe. "I_s" is the ion saturation current.

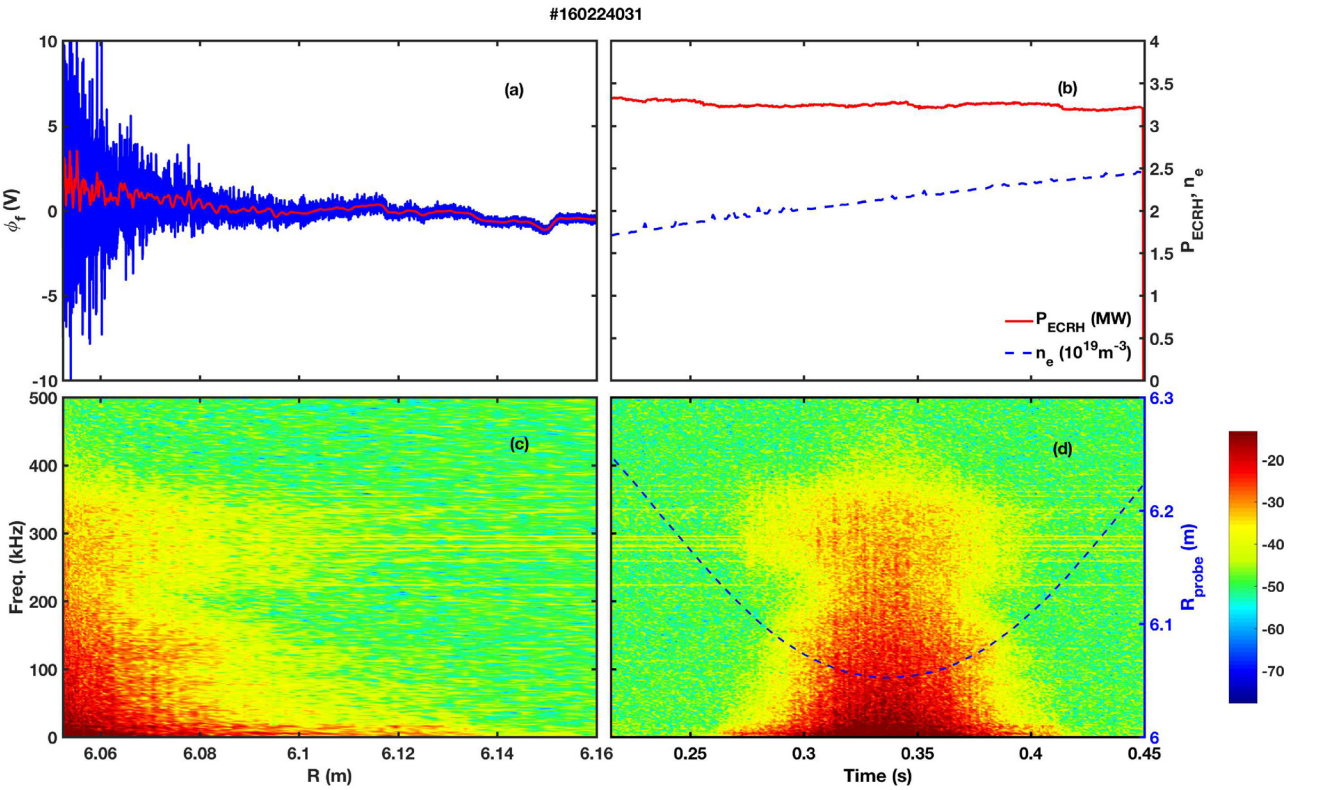

FIG. 2. (a) The floating potential measured by the combined probe; (b) ECRH heating power and line integrated density; (c) the radial distribution of auto-correlation spectra for floating potential; and (d) the time evolutions of the spectra for floating potential. The blue dashed line in (d) is the radial position of the combined probe.

by the combined probe head, with the blue line as the raw signal and the red line denoting the mean value. The amplitudes of floating potential fluctuations start to increase at the major radius around 6.15 m and is enhanced significantly near $R = 6.08$ m. Figures 2(c) and 2(d) show the auto-correlation power density (ACPD) of floating potential. For the spectral of floating potential, ACPD starts to rise at $R = 6.15$ m and increases to a relatively high level near $R = 6.08$ m, which is similar to the variation of raw signal in Fig. 2(a). The electrostatic fluctuations are dominated by a low frequency turbulence, which is well below 100 kHz when the combined probe is close to the LCFS. There is also a broadband spectrum in the high frequency range between 240 and 380 kHz, whose ACPD is much lower than that of the low frequency dominant fluctuations.

To gain further insight into the properties of the fluctuations from the floating potential, we have investigated their self-similar character via fitting the spectrum power decay function $S \propto f^{\alpha}$, where S is the ACPD. As illustrated in Fig. 3, two similar discharges are selected to illustrate the influence of trim coils on the SOL turbulence, with the trim coils switched off for discharge 160224028 and switched on for discharge 160224031. The auto-correlation power of floating potential ϕ_f is shown in Figs. 3(a)–3(c), with $R = 6.13$, 6.09, and 6.05 m, respectively. When the trim coils are switched on, the ACPD of ϕ_f reduces obviously, indicating a strong turbulence mitigation in the SOL caused by the error fields, especially in the near SOL. In the far SOL, the amplitude of ACPD is about two orders smaller than that in the near SOL. In Fig. 3(a), between 3 and 40 kHz frequency range, the

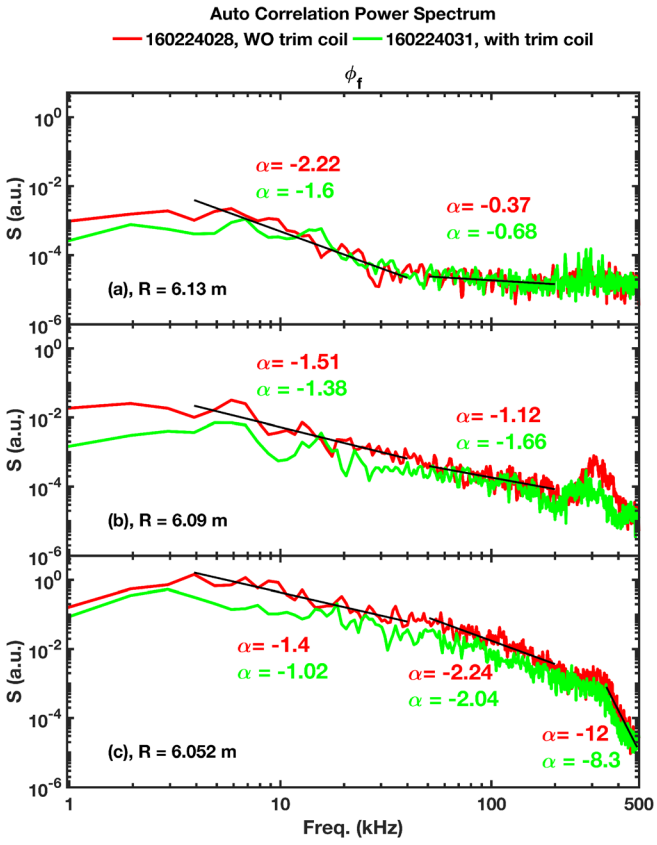

FIG. 3. The frequency spectrum $S(f)$ of fluctuations from floating potential ϕ_f. In (a)–(c), the power law decay factor α of $S \propto f^{\alpha}$ is given for the floating potential spectrum by fitting the data points covered by the solid black line. The red line is discharge 160224028 with trim coil switched off, while the green line is discharge 160224031 with trim coil switched on.

relationships between S and f are about $S \propto f^{-2.22}$ and $S \propto f^{-1.6}$ for discharges 160224028 and 160224031, respectively, and the intensities of ACPD decrease sharply to a very low level between 10 and 40 kHz. From 50 kHz to 200 kHz, the ACPD decreases slowly with $\alpha = -0.37$ and –0.68 for the two discharges. Note that a low frequency coherent mode (near 7 kHz) exhibits in the auto-correlation spectrum of the floating potential in the far SOL, but becomes weak in the near SOL, as shown in the ACPD of the floating potential for the discharge 160224028. In the case of $R = 6.09$ m, the power law decay factor α in the frequency range of 3–40 kHz is about –1.51 and –1.38, while in the frequency range of 50–200 kHz is –1.12 and –1.66 for both discharges. The broadband spectrum between 240 and 380 kHz starts to peak in the ACPD. In the near SOL with $R = 6.05$ m (2 cm outside the LCFS), the decay factor in the frequency regime of 3–40 kHz is $\alpha = -1.4$ and –1.02, while $\alpha = -2.24$ and –2.04 in the range of 50–200 kHz for both discharges, respectively. In the high frequency range of 350-490 kHz, the ACPD of both discharges exhibits similar decay trend, with $\alpha = -12$ and –8.3, respectively.

The interpretation of the power decay law has been investigated for a long time. According to the sand pile modelling and some experimental results: (i) in the low frequency part, a decay factor near $\alpha = 0$ reflecting global events with extremely large scales; (ii) in the high frequency, the decay factor $\alpha \geq -2$ signifying the small-scale individual events; (iii) the intermediate range with $\alpha = -1$ indicating the overlapping of avalanche transport.[19–23] In the near SOL, there is a low frequency region with α close to –1, as shown in Fig. 3(c), which is similar with the previous work on W7-AS, where a decay factor about –1 is found in the frequency range from 2 to 100 kHz near the separatrix.[23] This $\alpha = -1$ region could be induced by the avalanche transport. Besides, the nonlinear interaction between the velocity shear of background plasma and fluctuations could also generate this $\alpha = -1$ scaling.[24,25] In addition, in the high frequency range of 50–200 kHz, the decay factor α is about –2, indicating that the small-scale turbulence is dominant.

Figure 4 presents the probability density functions (PDFs) of the floating potential fluctuations $\tilde{\phi}_f$ for the shot 160224028 with the trim coil switched off. The linear trend of the raw signal has been removed before calculating the PDFs. The PDFs are fitted by a Gaussian distribution $f(x) = ae^{-bx^2}$ and a Laplace distribution $f(x) = ae^{-b|x|}$, respectively. In the far SOL, the PDFs follow Gaussian distribution. At $R = 6.09$ m, most of the fluctuations obey the Gaussian distribution, except the positive tail on the right side that is much higher than the Gaussian curve. Moreover, the PDFs reveal a strong asymmetry of the tails on both the left and the right sides. In the near SOL with $R = 6.052\,m$, the PDFs consist with the Gaussian fitting when $|\tilde{\phi}_f/\sigma| < 2$, while there are elevated tails for both positive and negative fluctuations compared to the Gaussian distribution. In Figs. 4(b) and 4(c), the elevated tails are located between the Gaussian and Laplace distributions. The skewness at all the three radial locations is also listed in Fig. 4, with a maximum value of 0.557 at $R = 6.09$ m, indicating the positive skewness. The kurtosis in the three locations is from 3.14 to 3.8,

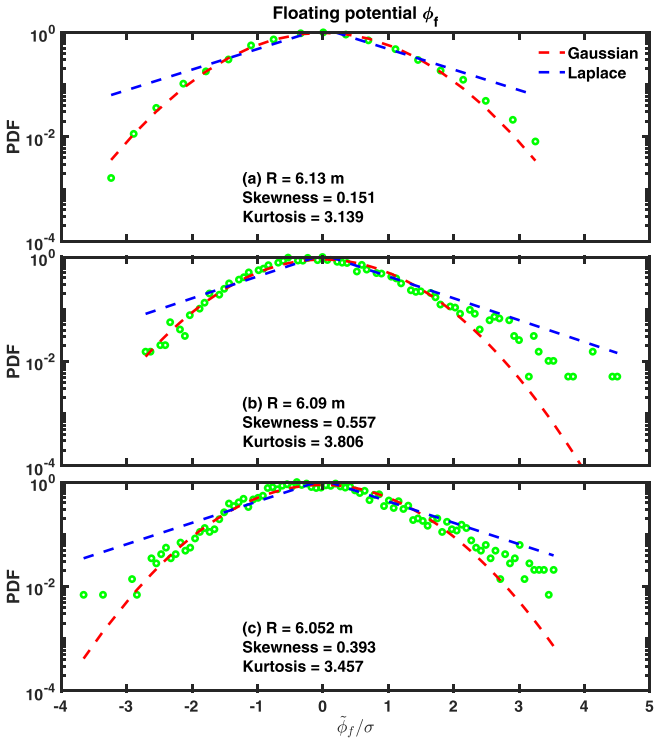

FIG. 4. The probability density functions of floating potential fluctuations at three radial positions for shot 160224028. $\tilde{\phi}_f = \phi_f - \langle \phi_f \rangle$ is the fluctuation level, and σ is the corresponding standard deviation. The PDFs are fitted by a Gaussian distribution and a Laplace distribution, as shown in the red and blue dashed lines, respectively. The skewness and kurtosis of each radial location are listed in each panel.

close to the Gaussian distribution with kurtosis = 3. According to a modelling of Hasegawa-Wakatati turbulence, the PDFs of large events are well approximated by the Laplace distribution, while small events often exhibit a Gaussian distribution.[24] In the near SOL, the small scale turbulence is one candidate for the power decay law $S \propto f^{-2}$ and the Gaussian distribution when $|\tilde{\phi}_f/\sigma| < 2$; while the large scale events, such as avalanche transport and coherent structures, could contribute to the $S \propto f^{-1}$ decay factor and the elevated tails in PDFs. In Fig. 6(b), there are some coherent structures in the near SOL, which may relate to these spectral characteristics. However, more detailed works are needed to study the energy cascades among different scales turbulence in the future.

The turbulence decorrelation time is derived from the e-folding time of auto-correlation function of the floating potential, as shown in Fig. 5. In the near SOL region, the decorrelation time for discharges of 160224028 and 160224031 is about $\tau_c = 25$ and 12 μs, respectively. The auto-correlation coefficient can be fitted by $f(t) = e^{-t/\tau_d}$, and the exponential decay factor τ_d is 31.7 and 14 s for these two shots. For shot 160224028, the fitting decay factor τ_d is larger than the decorrelation time τ_c, mostly due to the slow decreasing of the auto-correlation coefficient in the region of $13\,\mu s < \tau_{lag} < 110\,\mu s$. Typical decorrelation time from other fusion plasma is about 10–30 μs, which is similar to our experimental results.[11,21,26,27] The discharge with the trim coils switched on has smaller decorrelation time, and the auto-correlation function decays to a very low level at $\tau_{lag} \approx 40\,\mu s$, while the

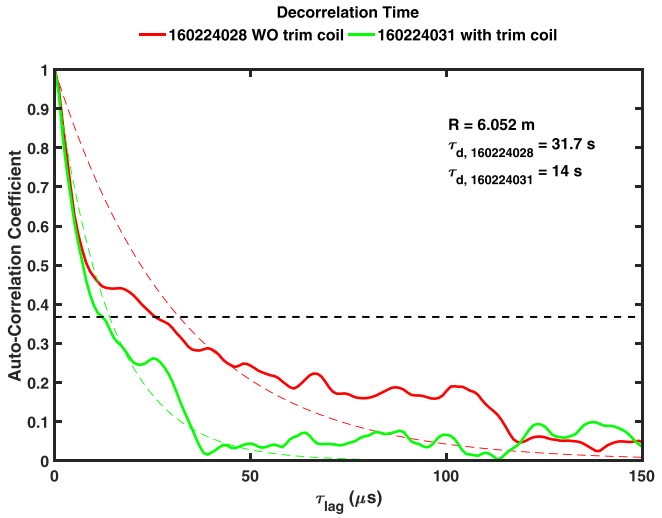

FIG. 5. The auto-correlation function of the floating potential for discharges 160224028 and 160224031. The auto-correlation coefficient is fitted by $f(t) = e^{-t/\tau_d}$, as illustrated in the dashed lines.

discharge without trim coil has a decaying tail with a weak correlation over 100 μs, demonstrating the existence of long time correlations, which is probably caused by large scale of bursts in the turbulence intermittency. Note that its correlation level is not high due to their small population and low occurrence frequency, but their contribution to radial transport could be large because of their big size and long lifetime.

B. Cross-correlation spectrum

The cross-correlations have been analyzed between two floating potential pins "ϕ_{fl}" and "ϕ_p" separated by 5.2 mm poloidally for discharge 160224028. The cross-correlation power density (CCPD) is presented in Fig. 6(b), exhibiting a strong power density below 100 kHz. A coherent mode near 7 kHz can be seen obviously when $R < 6.14$ m. The intensity of CCPD increases to a relatively high level when $R < 6.08$ m due to the sharp rise of fluctuation amplitude in floating potentials in this region. In addition, there is a weak broadband spectrum in the frequency range of 240–380 kHz. In Fig. 6(a), significantly high cross-correlation coefficient γ is observed for the low frequency coherent mode and the high frequency broadband, and both structures have clear radial dependence. The low frequency coherent mode is highlighted in the radial region of 6.09 m $< R <$ 6.14 m, while the broadband spectrum is highlighted when $R < 6.12$ m. For both structures, the cross-correlation phase is near zero, especially for the broadband. Note that the frequency of the broadband spectrum has no changes in the ECRH heating power range of 2–4 MW and line integrated density regime of 1–3 $\times$ 10^{19}m^{-2}. The characteristics of the low frequency electromagnetic coherent mode (EMCM) have been investigated in detail in our previous work.[28]

C. Statistical characteristics of the SOL turbulence

In this section, the turbulence properties including wave number, correlation length, and propagation are analyzed through the two-point cross-correlation technique that is usually used for the Langmuir probe data analysis.[29,30] In order to increase the sampling points for each calculation, a series of radial scan experiments are carried out to measure the fluctuations in a fixed position of the combined probe for each discharge. Nine discharges from 160223023 to 160223031 having identical plasma conditions are selected,

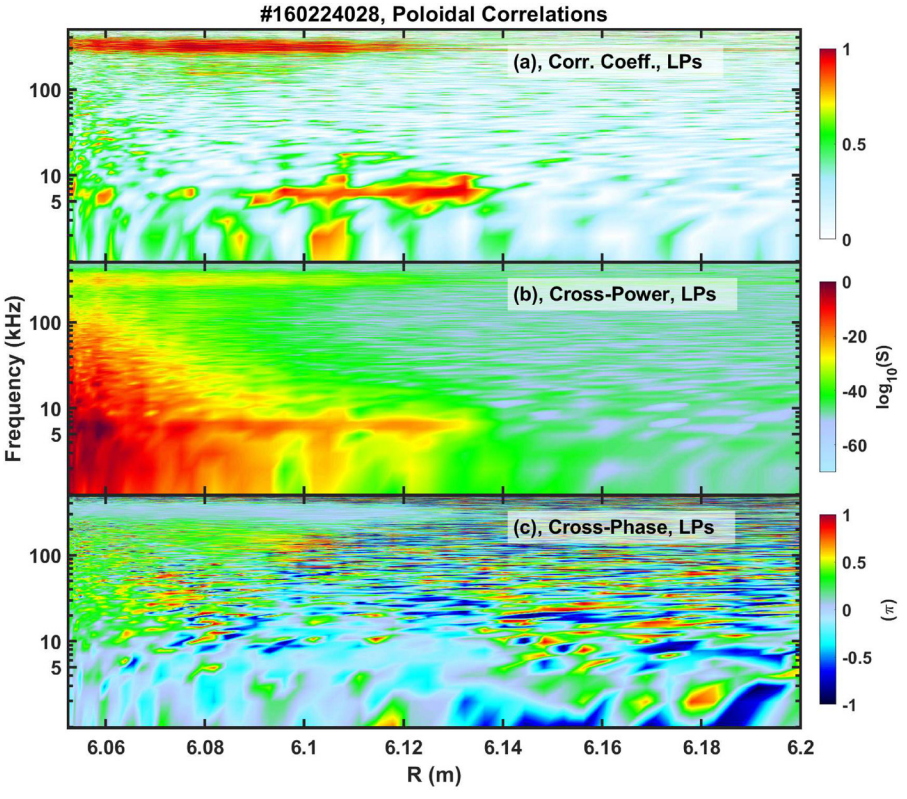

FIG. 6. The cross-correlation between two poloidally separated floating potentials. (a) Cross-correlation coefficient; (b) cross-correlation power; and (c) cross-correlation phase.

with ECRH heating power of 2 MW and line integrated density around $1.5–2 \times 10^{19}\mathrm{m}^{-2}$ during the interesting time period. The normalized poloidal cross-correlation spectral density $S(k_\theta, f)$ as a function of the poloidal wave number and frequency is obtained from the two poloidal separated floating potentials "ϕ_{f1}" and "ϕ_p," as shown in Fig. 7. Clear turbulence structures start to appear at $R \approx 6.135$ m, and the bright spectrum has almost zero k_θ and a low dominant frequency (<30 kHz). In Figs. 7(4) and 7(5), the frequency range of the bright spectrum increases to 40 and 60 kHz, but the distribution of the spectral density is almost symmetric about $k_\theta = 0$. Distinct statistical dispersion relation is observed when $R \leq 6.075$ m, and the main power is concentrated in the low frequency range, especially below 60 kHz in the near SOL. Within this high spectral power region, the turbulence group velocity $V_{group} = d\omega/dk$ estimated from the slope of $S(k_\theta, f)$ in the space of k_θ and f increases gradually from about 0.27 km/s at $R = 6.075$ m to about 0.56 km/s at $R = 6.046$ m (1.6 cm outside the LCFS), along the direction of the ion diamagnetic drift ($\omega_{*,i}$) in the laboratory frame. It should be pointed out that the spectral density of the high frequency broadband spectrum (240–380 kHz) is much weaker than the low frequency turbulence in the near SOL.

To illustrate the main characteristics of the spectrum $S(k_\theta, f)$, usually a conditional spectrum defined by $S(k_\theta|f) = S(k_\theta,f)/S(f) = S(k_\theta,f)/\sum_{k_\theta} S(k_\theta,f)$ is used, which is normalized by the power at each frequency. The poloidal spectrum $S(k_\theta|f)$ is shown in Fig. 8 for the entire frequency range. Above 100 kHz, the spectral density has a symmetrical distribution in both ion diamagnetic drift ($\omega_{*,i}$) and electron diamagnetic drift ($\omega_{*,e}$) directions, including the high frequency broadband. In the dominant spectral power region (f < 100 kHz), the main power is on the side of $k_\theta > 0$ in the near SOL, i.e., the turbulence propagates in the direction of $\omega_{*,i}$. When integrating the spectral power density over the whole frequency (or wave number) range, the $S(k)$ [or $S(f)$] is obtained, as displayed in Fig. 9. It is noticed that the radial statistical characteristics are derived from the two floating potentials "ϕ_{f1}" and "ϕ_{f3}" which are separated by 6 mm radially. Same as in Figs. 7 and 8, the symmetrical $S(k_\theta)$ changes to $\omega_{*,i}$ direction favoured around $R = 6.075$ m. Noted in the near SOL, $S(k_\theta)$ has a more balanced power distribution among k_θ from -0.5 to 3.5. Similar to $S(k_\theta)$, the radial spectral power $S(k_r)$ is also concentrated on the side with $k_r > 0$ when $R < 6.066$ m, i.e., the turbulence propagates outwards in the near SOL. From the $S(f)$ of both poloidal and radial correlations in Figs. 9(c) and 9(d), we can see that most power density is located in the frequency range below 60 kHz, especially below 20 kHz. The low frequency coherent mode also appears in $S(f)$ and is strong in the radial location of $R = 6.09$ to 6.14 m, indicating its dependence on magnetic topology.

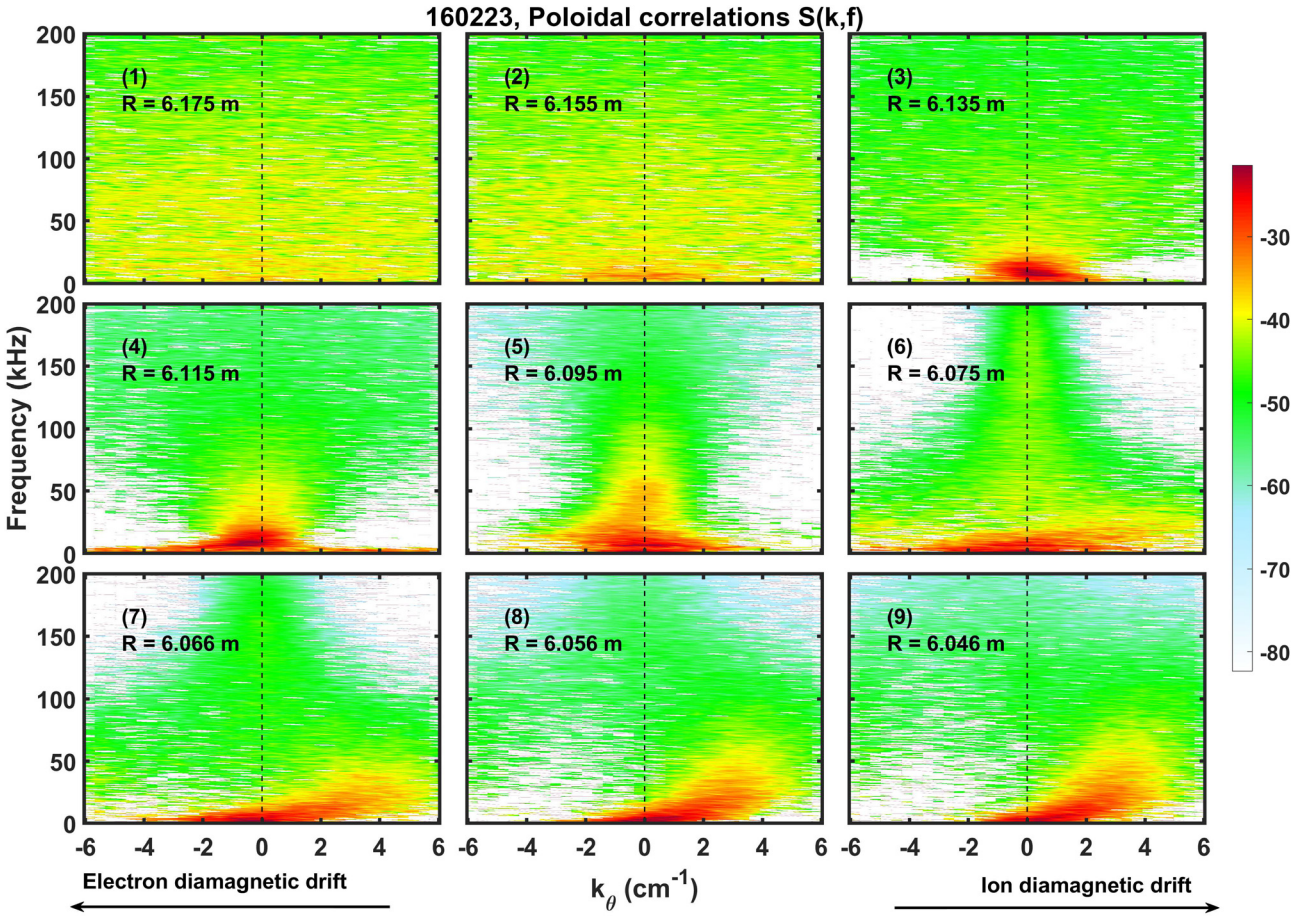

FIG. 7. The normalized poloidal cross-correlation spectral density $S(k_\theta, f)$ of the nine discharges in the experimental day 20160223. The radial position of the combined probe is given in each panel, with the LCFS located at $R = 6.03$ m.

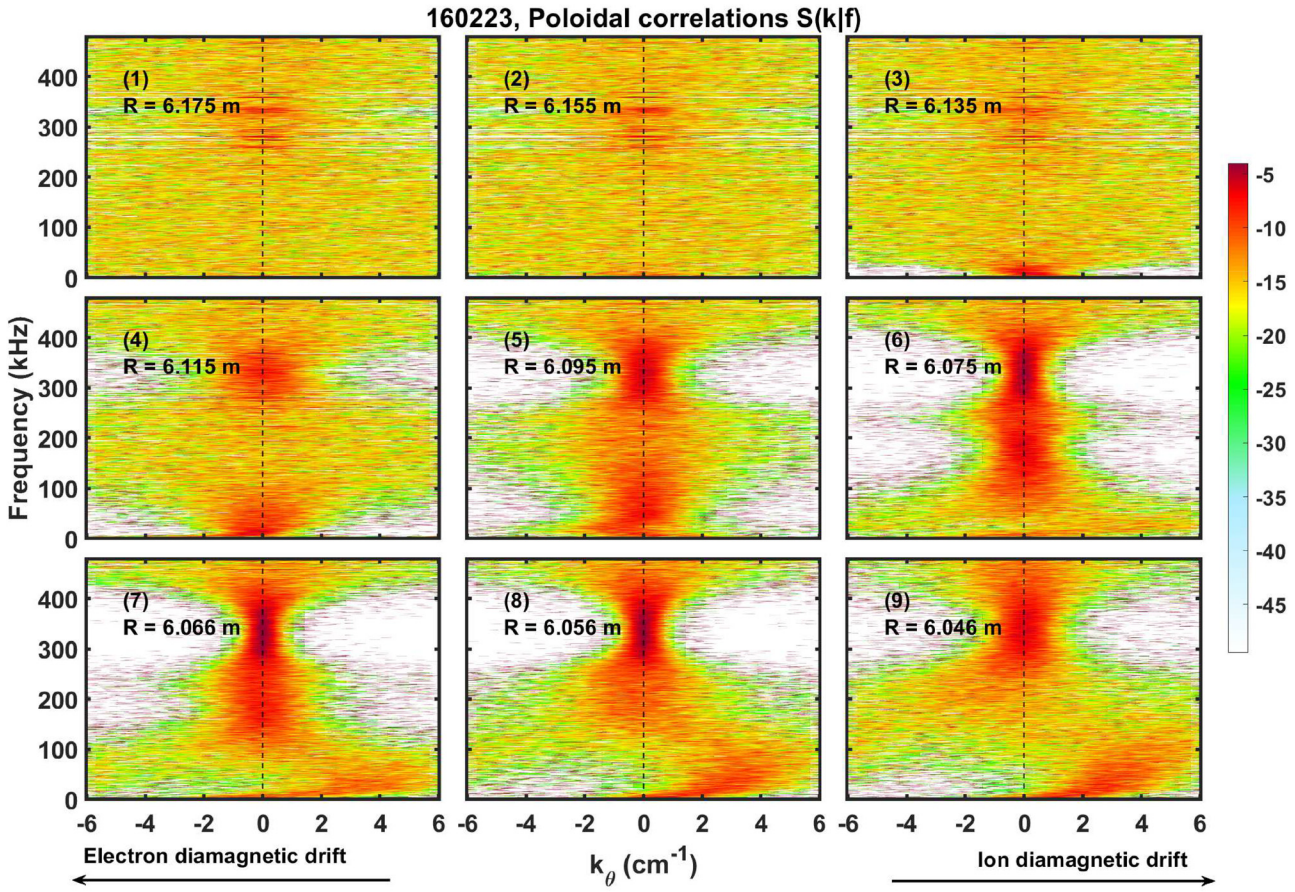

FIG. 8. The poloidal conditional spectral density $S(k_\theta|f)$ of the nine discharges in the experimental day 20160223.

The detailed poloidal statistical parameters are given in Fig. 10 to shed more light on the poloidal turbulence structures. Here, the frequency range (1–200 kHz) containing the main spectral power density is used for the calculations. Note the discharge 160224028 has a higher ECRH heating power of 3.3 MW. Figure 10(c) gives the cross-correlation coefficient of the calculation, which is well above 0.5 when the probe is plunging inside the plasma. As measured by the floating potential and its ACPD, the probe starts to touch plasma around $R = 6.15$ m, and consequently, the statistical parameters have sharp changes in this region. The coefficient peaks at about $R = 6.11$ m, especially for discharge

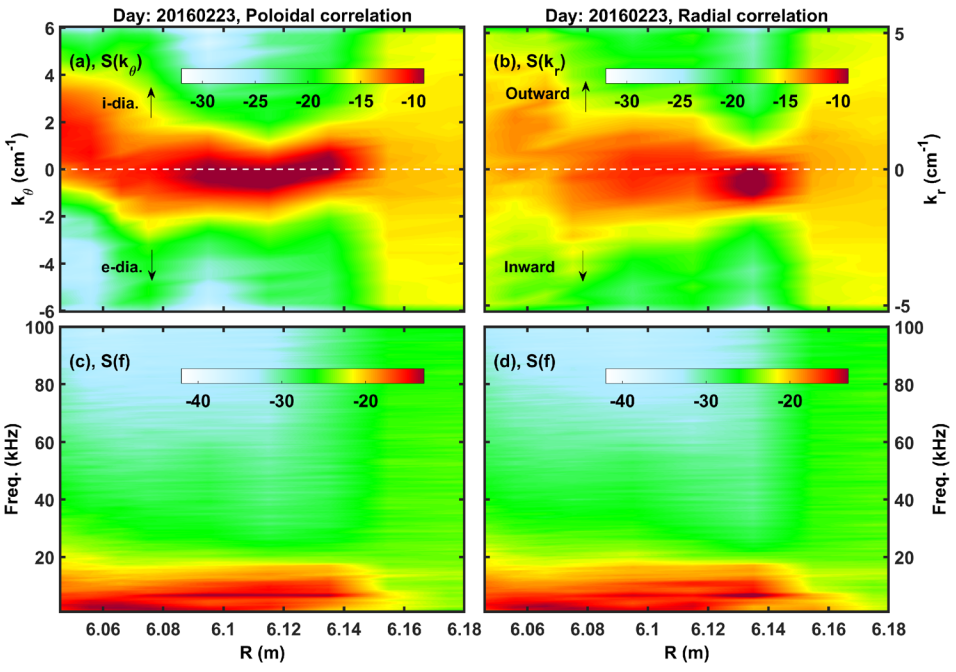

FIG. 9. The radial dependence of $S(k)$ and $S(f)$ in both poloidal and radial directions. (a) $S(k_\theta)$; (b) $S(k_r)$; (c) the integral of $S(k_\theta, f)$ over the k_θ space; and (d) the integral of $S(k_r, f)$ over the k_r space.

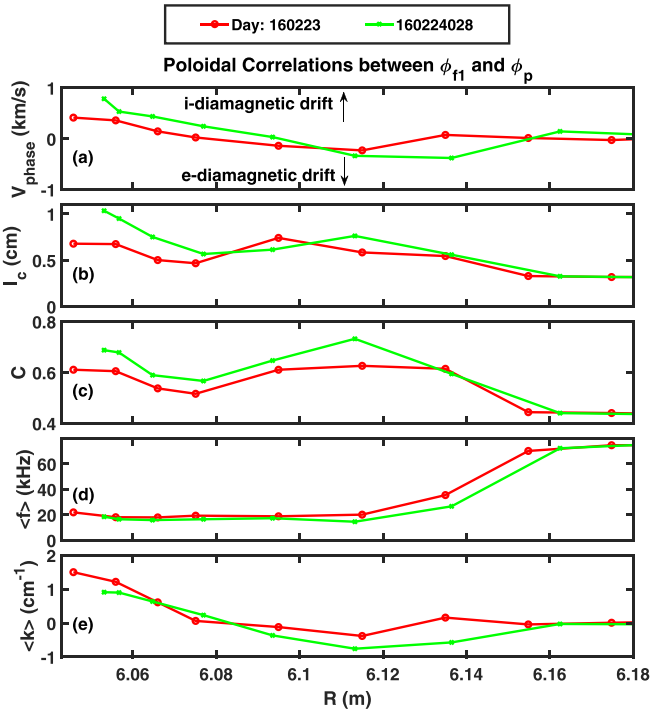

FIG. 10. The poloidal statistical parameters. (a) Turbulence phase velocity; (b) correlation length; (c) cross-correlation coefficient; (d) weighted frequency; and (e) weighted wave number. The discharges in experimental day 20160223 has P_{ECRH} = 2 MW, while P_{ECRH} of discharge 160224028 is 3.3 MW.

160224028, also have a slight increase in the near SOL. The weighted frequency $\langle f\rangle = \sum fS(f)$ is shown in Fig. 10(d), illustrating that $\langle f\rangle$ decreases from 70 kHz when R > 6.15 m to about 20 kHz when $R < 6.11$ m. In the most SOL, the spectral power is mainly in this low frequency region. Figure 10(e) presents the weighted poloidal wave number $\langle k\rangle = \sum_f \bar{k}(f)S(f)$, where $\bar{k}(f) = \sum_k kS(k|f)$ is the power-averaged dispersion relation. From $R = 6.12$ m, $\langle k_\theta\rangle$ increases with decreasing R-R_{LCFS} and changes its value from negative to positive, i.e., from the direction $\omega_{*,e}$ to $\omega_{*,i}$. The increasing value of $\langle k_\theta\rangle$ means that the contribution from small-scale turbulence is enhanced when close to the LCFS. The negative $\langle k_\theta\rangle$ from major radius 6.1–6.14 m of discharge 160224028 is also noticeable. The turbulence poloidal correlation length is shown in Fig. 10(b), defined by $l_c = 1/\langle\sigma_k\rangle$, where the wavenumber spectral width is given by $\langle\sigma_k^2\rangle = \sum_f \bar{\sigma}_k^2 S(f) = \sum_f S(f)\left\{\sum_k \left[k-\bar{k}(f)\right]^2 S(k|f)\right\}$. The turbulence poloidal correlation length is about 5–10 mm in the SOL and has a similar radial profile as the correlation coefficient. The turbulence phase velocity is calculated by $V_{phase} = \sum_{k,f} 2\pi fS(k,f)/k$.[31] As shown in Fig. 10(a), V_{ph} increases gradually when close to the LCFS in the near SOL, and the maximum speed is about 0.4 km/s for the 2 MW discharges and 0.7 km/s for the 3.3 MW discharge, both along the $\omega_{*,i}$ direction. There is a negative V_{phase} in the radial region of R=6.11–6.14 m, especially for the 3.3 MW discharge. The poloidal correlation length and phase velocity are consistent with these measured in similar plasmas.[32–34] In consequence, the poloidal turbulence behaviours in the near SOL largely depend on the low frequency turbulence which propagates in the $\omega_{*,i}$ direction in the laboratory frame. In the radial region of R=6.11–6.14, the high correlation coefficient and negative phase velocity for the discharge of 160224028 are caused by the electromagnetic coherent mode which propagates in the $\omega_{*,e}$ direction in both the laboratory frame and the plasma frame.[28]

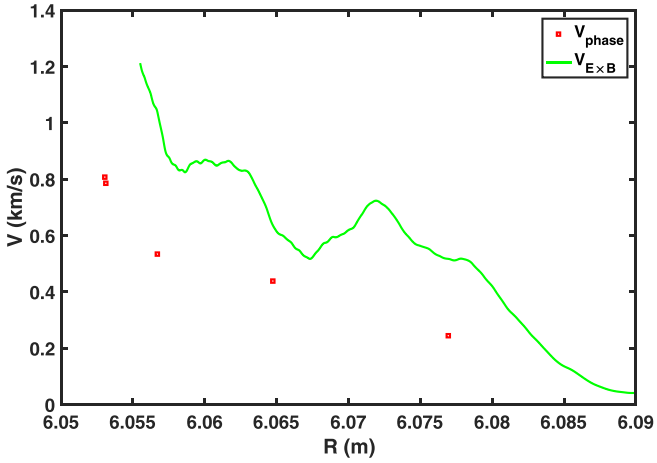

FIG. 11. The $\boldsymbol{E}\times\boldsymbol{B}$ drift velocity from discharge 160228016 and turbulence phase velocity from discharge 160228028.

The turbulence poloidal phase velocity in the lab frame is considered as the sum of electric drift $V_{E\times B} = E_r/B_{parallel}$ and some plasma-frame phase velocity $V_{plasma\,frame}$.[35] As a result, the turbulence phase velocity is usually used to estimate the radial electric field. In our experiment, a discharge of 160224016 selected to calculate the $E\times B$ drift velocity has the same plasma condition with the discharge 160224028 except that the combined probe is operated in the triple-probe model which can measure the radial profile of electron temperature. The radial electric field is derived from $E_r = -d(\phi_f + 2.8T_e)/dR$. The turbulence phase velocity and $E\times B$ drift velocity are shown in Fig. 11, and $V_{E\times B}$ is a little larger than V_{phase}, indicating this estimation of E_r is acceptable in the SOL plasma of W7-X.

IV. CONCLUSION

The SOL turbulence characteristics have been measured in the first experimental campaign of W7-X by the combined probe. In this paper, the preliminary experimental results about the SOL turbulence properties are introduced, aiming to give a reference in the limiter configuration on W7-X. In the standard limiter configuration of OP1.1, significant electrostatic fluctuations can be found when the major radius $R < 6.08$ m which is about 5 cm outside the LCFS. In this near SOL region, the fluctuation power is concentrated in the frequency regime below 100 kHz, as demonstrated in the auto-correlation power spectrum and poloidal cross-correlation spectrum power of floating potentials. In the low frequency range (below 40 kHz) in the near SOL, the spectrum power law decay factor α is around -1, which could be induced by the avalanche interactions, such as large-scale bursts and background fluctuations. The nonlinear interaction between fluctuations velocity shear and background

plasma velocity shear is another candidate for this $\alpha = -1$ power law decay. Between the frequency range from 50 to 200 kHz, the factor α is about -2, which signifies that small-scale turbulence is dominant in this region. Besides, a high frequency broadband spectrum is observed between 240 and 380 kHz, which has much weaker fluctuation power than that in the dominant frequency but has higher cross-correlation coefficient. When the trim coils are turned on, the fluctuation level is suppressed significantly. In the near SOL, the probability density functions (PDFs) of the floating potential fluctuations exhibit a Gaussian distribution in most fluctuation levels, while display elevated tails. The two-point cross-correlation technique is used to analyze the turbulence statistical parameters. The poloidal correlation power spectrum $S(k_\theta, f)$ exhibits an explicit dispersion relation in the near SOL, propagating along the ion diamagnetic drift direction with a speed about 0.56 km/s in the laboratory frame for the frequency region below 100 kHz. Although the broadband also has a high level of the conditional spectral density $S(k_\theta|f)$, the power spectrum $S(k_\theta, f)$ is relatively weak, indicating the low frequency turbulence could play the main role in turbulence transport. When the probe moves close to the LCFS, the weighted poloidal wave number increases slightly in the direction of ion diamagnetic drift. The SOL turbulence poloidal correlation length is between 5 and 10 mm and could be longer when getting closer to the LCFS. The turbulence phase velocity between 1 and 200 kHz is derived, which is around 0.5–1 km/s in the near SOL and a little larger in the higher heating power cases. This turbulence phase velocity is comparable with the poloidal $E \times B$ drift velocity, while the former one is a bit smaller. In addition, a low frequency electromagnetic coherent mode is observed in OP1.1, which has a clear structure in high heating power discharges and exhibits strong magnetic topology dependence. However, much more work is required to give a comprehensive physical image of edge turbulence in W7-X, including the radial heat and particle transport driven by fluctuations and much deeper measurement of turbulence. Hence, a new combined probe head has been developed to measure more information about electrostatic and magnetic fluctuations, which will contribute to further study the edge turbulence structures in W7-X.

ACKNOWLEDGMENTS

This work has been carried out within the framework of the EUROfusion Consortium, has received funding from the Euratom research and training programme 2014–2018 under Grant Agreement No. 633053, and was supported by the National Natural Science Foundation of China under Grant Nos. 11405213 and 11605235. The views and opinions expressed herein do not necessarily reflect those of the European Commission.

[1]E. J. Doyle, W. A. Houlberg, Y. Kamada, V. Mukhovatov, T. H. Osborne, A. Polevoi, G. Bateman, J. W. Connor, J. G. Cordey, T. Fujita, X. Garbet, T. S. Hahm, L. D. Horton, A. E. Hubbard, F. Imbeaux, F. Jenko, J. E. Kinsey, Y. Kishimoto, J. Li, T. C. Luce, Y. Martin, M. Ossipenko, V. Parail, A. Peeters, T. L. Rhodes, J. E. Rice, C. M. Roach, V. Rozhansky, F. Ryter, G. Saibene, R. Sartori, A. C. C. Sips, J. A. Snipes, M. Sugihara, E. J. Synakowski, H. Takenaga, T. Takizuka, K. Thomsen, M. R. Wade, H. R. Wilson, I. T. P. T. Grp, and I. C. D. Modellin, Nucl. Fusion **47**, S18 (2007).
[2]J. Wesson and D. J. Campbell, *Tokamaks* (Oxford University Press, Oxford, New York, 2011).
[3]W. Horton, Rev. Mod. Phys. **71**, 735 (1999).
[4]H. Q. Wang, G. S. Xu, B. N. Wan, S. Y. Ding, H. Y. Guo, L. M. Shao, S. C. Liu, X. Q. Xu, E. Wang, N. Yan, V. Naulin, A. H. Nielsen, J. J. Rasmussen, J. Candy, R. Bravenec, Y. W. Sun, T. H. Shi, Y. F. Liang, R. Chen, W. Zhang, L. Wang, L. Chen, N. Zhao, Y. L. Li, Y. L. Liu, G. H. Hu, and X. Z. Gong, Phys. Rev. Lett. **112**, 185004 (2014).
[5]C. A. Michael, F. Zhao, B. Blackwell, M. F. J. Vos, J. Brotankova, S. R. Haskey, B. Seiwald, and J. Howard, Plasma Phys. Controlled Fusion **59**, 024001 (2017).
[6]Z. Yan, G. R. McKee, R. Fonck, P. Gohil, R. J. Groebner, and T. H. Osborne, Phys. Rev. Lett. **112**, 125002 (2014).
[7]P. H. Diamond, S. I. Itoh, K. Itoh, and T. S. Hahm, Plasma Phys. Controlled Fusion **47**, R35 (2005).
[8]P. Manz, M. Ramisch, U. Stroth, V. Naulin, and B. D. Scott, Plasma Phys. Controlled Fusion **50**, 035008 (2008).
[9]M. Otte, D. Assmus, C. Biedermann, S. Bozhenkov, T. Brauer, A. Dudek, J. Geiger, G. Kocsis, S. Lazerson, T. S. Pedersen, F. Schauer, T. Szepesi, and B. Standley, and W.-X. Team, Plasma Phys. Controlled Fusion. **58**, 064003 (2016).
[10]T. Windisch, A. Kramer-Flecken, J. L. Velasco, A. Konies, C. Nuhrenberg, O. Grulke, T. Klinger, and W.-X. Team, Plasma Phys. Controlled Fusion. **59**, 105002 (2017).
[11]A. Krämer-Flecken, T. Windisch, W. Behr, G. Czymek, P. Drews, G. Fuchert, J. Geiger, O. Grulke, M. Hirsch, M. Knaup, Y. Liang, O. Neubauer, E. Pasch, J. L. Velasco, and W.-X. Team, Nucl. Fusion **57**, 066023 (2017).
[12]G. M. Weir, O. Grulke, H. J. Hartfuss, M. Hirsch, N. B. Marushchenko, H. Tsuchiya, T. Windisch, and W.-X. Team, in *43rd EPS Conference on Plasma Physics*, *Leuben, Belgium* (2016), p. P4.009.
[13]U. Höfel, S. Bozhenkov, G. Fuchert, J. Geiger, H. J. Hartfuss, M. Hirsch, F. Köster, H. Maaßberg, N. B. Marushchenko, E. Pasch, S. Schmuck, T. Stange, H. Tsuchiya, Y. Turkin, J. L. Velasco, G. M. Weir, R. Wolf, and W.-X. Team, in *43rd EPS Conference on Plasma Physics*, *Leuben, Belgium* (2016), p. P4.008.
[14]K. Rahbarnia, T. Andreeva, A. Cardella, B. B. Carvalho, M. Endler, D. Hathiramani, J. Geiger, O. Grulke, S. Lazerson, U. Neuner, J. Svensson, H. Thomsen, A. Werner, and W.-X. Team, in *43rd EPS Conference on Plasma Physics*, Leuben, Belgium (2016), p. P4.011.
[15]G. Satheeswaran, K. P. Hollfeld, P. Drews, D. Nicolai, O. Neubauer, B. Schweer, and O. Grulke, Fusion Eng. Des. **123**, 699 (2017).
[16]D. Nicolai, V. Borsuk, P. Drews, O. Grulke, K. P. Hollfeld, T. Krings, Y. Liang, C. Linsmeier, O. Neubauer, G. Satheeswaran, B. Schweer, G. Offermanns, and W.-X. Team, Fusion Eng. Des. **123**, 960 (2017).
[17]Y. Liang, O. Neubauer, R. Konig, M. Krychowiak, B. Schweer, P. Denner, M. Rack, D. Reiter, Y. Feng, A. Kramer-Flecken, P. Drews, F. Hasenbeck, S. Liu, Y. Gao, E. H. Wang, Y. Wei, M. Dostal, L. Li, N. Wang, J. Geiger, Y. Suzuki, S. Sereda, P. Borner, A. C. Weger, W. Biel, S. Brezinsek, A. Charl, G. Czymek, D. Hoschen, F. Effenberg, O. Grulke, D. Nicolai, H. T. Lambertz, O. Marchuk, O. Schmitz, K. P. Hollfeld, M. Knaup, G. Offermanns, G. Satheeswaran, A. Terra, J. Thomas, T. S. Pederson, U. Samm, C. Linsmeier, and W.-X. Team, Nucl. Fusion **57**, 066049 (2017).
[18]P. Drews, Y. Liang, S. Liu, A. Krämer-Flecken, O. Neubauer, J. Geiger, M. Rack, D. Nicolai, O. Grulke, C. Killer, N. Wang, A. Charl, B. Schweer, P. Denner, M. Henkel, Y. Gao, K. Hollfeld, G. Satheeswaran, N. Sandri, D. Höschen, and W. X. Team, Nucl. Fusion **57**, 126020 (2017).
[19]R. Sanchez, B. P. van Milligen, D. E. Newman, and B. A. Carreras, Phys. Rev. Lett. **90**, 185005 (2003).
[20]R. Sanchez, D. E. Newman, and B. A. Carreras, Phys. Rev. Lett. **88**, 068302 (2002).
[21]Y. H. Xu, S. Jachmich, R. R. Weynants, and T. Team, Plasma Phys. Controlled Fusion. **47**, 1841 (2005).
[22]T. Hwa and M. Kardar, Phys. Rev. A **45**, 7002 (1992).
[23]B. A. Carreras, B. P. van Milligen, M. A. Pedrosa, R. Balbin, C. Hidalgo, D. E. Newman, E. Sanchez, M. Frances, I. Garcia-Cortes, J. Bleuel, M. Endler, C. Riccardi, S. Davies, G. F. Matthews, E. Martines, V. Antoni, A. Latten, and T. Klinger, Phys. Plasmas **5**, 3632 (1998).
[24]J. Anderson and B. Hnat, Phys. Plasmas **24**, 062301 (2017).
[25]C. M. Tchen, J. Res. Natl. Bur. Stand. **50**, 51 (1953).

[26]S. J. Zweben, J. L. Terry, B. LaBombard, M. Agostini, M. Greenwald, O. Grulke, J. W. Hughes, D. A. D'Ippolito, S. I. Krasheninnikov, J. R. Myra, D. A. Russell, D. P. Stotler, and M. Umansky, J. Nucl. Mater. **415**, S463 (2011).
[27]G. S. Xu, B. N. Wan, W. Zhang, Q. W. Yang, L. Wang, and Y. Z. Wen, Phys. Plasmas **13**, 102509 (2006).
[28]S. C. Liu, Y. Liang, P. Drews, A. Kramer-Flecken, X. Han, D. Nicolai, G. Satheeswaran, N. C. Wang, J. Q. Cai, A. Charl, J. Cosfeld, G. Fuchert, Y. Gao, J. Geiger, O. Grulke, M. Henkel, M. Hirsch, U. Hoefel, K. P. Hollfeld, D. Hoschen, C. Killer, A. Knieps, R. Konig, O. Neubauer, E. Pasch, K. Rahbarnia, M. Rack, N. Sandri, S. Sereda, B. Schweer, E. H. Wang, Y. L. Wei, G. Weir, T. Windisch, and W.-X. Team, Nucl. Fusion **58**, 046002 (2018).
[29]J. M. Beall, Y. C. Kim, and E. J. Powers, J. Appl. Phys. **53**, 3933 (1982).
[30]S. J. Levinson, J. M. Beall, E. J. Powers, and R. D. Bengtson, Nucl. Fusion **24**, 527 (1984).
[31]T. Uckan, C. Hidalgo, J. D. Bell, J. H. Harris, J. L. Dunlap, G. R. Dyer, P. K. Mioduszewski, J. B. Wilgen, C. P. Ritz, A. J. Wootton, T. L. Rhodes, and K. Carter, J. Nucl. Mater. **176**, 693 (1990).
[32]Y. Xu, M. Van Schoor, R. R. Weynants, S. Jachmich, M. Vergote, M. W. Jakubowski, P. Beyer, M. Mitri, B. Schweer, D. Reiser, B. Unterberg, K. H. Finken, M. Lehnen, R. Jaspers, and T. Team, Nucl. Fusion **47**, 1696 (2007).
[33]Y. Sun, Z. P. Chen, T. Z. Zhu, Q. Yu, G. Zhuang, J. Y. Nan, X. Ke, H. Liu, and J.-T. Team, Plasma Phys. Controlled Fusion **56**, 015001 (2014).
[34]C. Hidalgo, B. Goncalves, M. A. Pedrosa, C. Silva, R. Balbin, M. Hron, A. Loarte, K. Erents, G. F. Matthews, and R. Pitts, J. Nucl. Mater. **313**, 863 (2003).
[35]J. H. Yu, C. Holland, G. R. Tynan, G. Antar, and Z. Yan, J. Nucl. Mater. **363**, 728 (2007).